Korean J. Chem. Eng., 36(2), 236-247 (2019)
DOI: 10.1007/s11814-018-0207-5

pISSN: 0256-1115
eISSN: 1975-7220

Facile preparation of antifouling g-C_3N_4/Ag_3PO_4 nanocomposite photocatalytic polyvinylidene fluoride membranes for effective removal of rhodamine B

Yanhua Cui*, Lili Yang*, Minjia Meng,†, Qi Zhang**, Binrong Li***, Yilin Wu**, Yunlei Zhang**, Jihui Lang****, and Chunxiang Li**,†**

*School of Materials Science and Engineering, Jiangsu University, Zhenjiang 212013, China
**Institute of Green Chemistry and Chemical Technology, School of Chemistry and Chemical Engineering, Jiangsu University, Zhenjiang 212013, China
***School of Environment and Safety Engineering, Jiangsu University, Zhenjiang 212013, China
****Jilin Normal University, Changchun 130103, China
(*Received 23 September 2018 • accepted 6 December 2018*)

Abstract−A simplified strategy for facilely fabricating antifouling graphite carbon nitride/silver phosphate (g-C_3N_4/Ag_3PO_4) nanocomposite photocatalytic polyvinylidene fluoride (PVDF) porous membranes was developed for effective removal of rhodamine B (RhB). g-C_3N_4/Ag_3PO_4 heterojunction was strongly fixed to the interior of the PVDF membranes *via* phase inversion method. The membrane structure was analyzed by Fourier transform spectrophotometer (FT-IR). The morphology of the prepared membranes was investigated using scanning electron microscopy (SEM), EDX-mapping and atomic force microscopy (AFM), respectively. All prepared nanocomposite photocatalytic PVDF membranes exhibited a typically porous structure, and g-C_3N_4/Ag_3PO_4 nanocomposites were well dispersed inside the membranes. The obtained g-C_3N_4/Ag_3PO_4 heterojunction nanoparticle decorated PVDF membrane had a lower water contact angle of 79° and higher porosity of 85% than that of other two control membranes. The nanocomposite photocatalytic PVDF porous membranes had extremely high permeation flux over 1,083 $L \cdot m^{-2} \cdot h^{-1}$, and could be used for the removal of RhB. The removal efficiency of g-C_3N_4/Ag_3PO_4-PVDF membranes towards RhB solution under visible light irradiation reached 97%, higher than that of the pure PVDF membranes (41%) and g-C_3N_4-PVDF membranes (85%). Remarkably, the flux performance and flux recovery ratio (*FRR*) of membranes revealed that the g-C_3N_4/Ag_3PO_4-PVDF membranes could recover high flux after fouling, which presented better fouling resistance. Furthermore, the fabricated antifouling g-C_3N_4/Ag_3PO_4 nanocomposite photocatalytic PVDF porous membranes exhibited excellent recyclability. Therefore, it is expected that g-C_3N_4/Ag_3PO_4-PVDF membranes could provide an energy-saving strategy for effective removal of organic dyes wastewater and have a great potential for practical wastewater treatment in the future.

Keywords: g-C_3N_4/Ag_3PO_4 Heterojunction, PVDF Membranes, Removal RhB, Anti-fouling Properties

INTRODUCTION

Along with increasing environmental problems and water resource scarcity, the concentration for clean and abundant water resource as well as treatment of wastewater is continuously increasing [1,2]. The emission of organic dyes from textile industries is the main source of organic pollution worldwide, which could pose a serious threat to ecological balance and human health due to the great biotoxicity, possible mutagenic and carcinogenic effects [3]. Herein, it is of great significance to explore an efficient and energy-saving technique for removing organic dyes. Membrane separation technology with high efficiency, eco-friendliness, safety and low energy consumption is widely used in wastewater treatment to remove various water contaminants [4,5]. However, the inherent shortcoming for the extensive use of membrane technology is membrane fouling [6], which is caused by the irreversible deposition of compounds on the membrane surface, resulting in flux decline, higher energy consuming and a shorter membrane service life [7]. Moreover, traditional membrane separation has limitation in removing contaminants with smaller sizes than the membrane pores, which leads to effluent water with potential hazard [8]. Hence, it is urgent to develop a multifunctional membrane that can automatically overcome these disadvantages in membrane separation for water treatment [9].

Recently, the integration of membrane separation with photocatalysis has rendered an interchangeable route to overcome the aforementioned drawbacks in the membrane separation process [10,11]. And during this integrated process, the integrated membranes not only can efficiently degrade various pollutants into carbon dioxide and water, but also markedly enhance fouling resistance. For example, Wang et al. reported that photocatalytic nanocomposite membranes were designed through depositing polydopamine layer and Au-TiO_2 nanoparticles layer on the surface of PVDF membrane support for degradation of tetracycline [12]. Fischer et al. reported the directed synthesis of photoactive microfiltration membranes by the immobilization of TiO_2 nanoparticles on the surface of PVDF membrane for removal of drugs from water [13]. Xu et al. fabricated photocatalytic membrane incorporating nitrogen-doped graphene/

†To whom correspondence should be addressed.
E-mail: mmj@ujs.edu.cn, lcx@mail.ujs.edu.cn

TiO_2 nanocomposites *via* a non-solvent-induced phase-separation method to enhance photocatalytic performance and anti-fouling properties under both UV and sunlight [14]. Nevertheless, most of the photocatalytic membrane materials for the functional layer are primarily focused on TiO_2 based photocatalysts; TiO_2 only absorbed UV-light which occupied 5-7% of the solar spectrum. As a consequence, the TiO_2-based photocatalytic membrane generally exhibits poor membrane performance under visible light irradiation and requires high energy consumption because of the employment of UV light source, which greatly limits its practical applications [15,16]. Considering these drawbacks, constructing a highly efficient photocatalytic membrane that could directly utilize visible light for dye wastewater treatment is highly desirable.

Graphitic carbon nitride (g-C_3N_4) has been extensively studied as an attractive metal-free photocatalyst with a medium band gap (2.65 eV) because of its visible light response, proper band edges and excellent chemical stability for organic pollutant degradation, hydrogen production and oxygen reduction [17-19]. However, the photocatalytic activity of g-C_3N_4 is still limited by the fast recombination rate of photogenerated electron-hole pairs and insufficient photon absorption above 450 nm in pure g-C_3N_4, which results in low photocatalytic efficiency [20,21]. Therefore, some strategies have been proposed to enhance the photocatalytic activity of g-C_3N_4, such as mesoporous structure design [22], doping with metal or nonmetal elements (such as C, Ag, Au and Pt) [23,24], heterostructured nanocomposites fabrication [25,26] by integrating with other semiconductors. Among these methods, constructing a heterojunction photocatalyst is one of the efficient strategies; numerous semiconductor materials, such as TiO_2 [27], ZnO [28], CdS [29], Ag_3PO_4 [30] and GO [31], have been proposed to couple with g-C_3N_4 to efficiently facilitate the photogenerated electron-hole pairs separation. Ag_3PO_4 photocatalyst has been regarded as a promising candidate due to its excellent visible-light-driven photocatalytic activity for the degradation of organic pollutants and appropriate band position which can well match that of g-C_3N_4 to accelerate efficient photo-generated charge carrier separation. The quantum yield of oxygen generated of Ag_3PO_4 from the water oxidation catalyzed can reach 90%, which is observably higher than the 20% yield produced by other photocatalysts under visible light irradiation [32]. In addition, Ag_3PO_4-based nanocomposite photocatalysts have high visible light absorption and can accelerate the photo-generated charge carriers separation effectively because of their strong electric field at the interface and wide band-edge offset [33]. Meanwhile, g-C_3N_4 could act as an effective electron transporter and an electron acceptor; coupling g-C_3N_4 with Ag_3PO_4 to form g-C_3N_4/Ag_3PO_4 heterostructured nanocomposites showed high photocatalytic activity and stable structure. Ma et al. [34] designed highly efficient and stable visible-light-induced photocatalysts on exfoliated bentonite/g-C_3N_4/Ag_3PO_4 nanocomposites for practical applications in wastewater treatment. Sun et al. [35] reported the excellent visible light photocatalytic property of g-C_3N_4 nanocrystals decorated Ag_3PO_4 hybrids for degradation organic pollutant. Therefore, the incorporation of g-C_3N_4/Ag_3PO_4 into membranes may enable a feasible method for effectively increasing their hydrophilicity, permeability and anti-fouling capability for wastewater treatment by directly utilizing the visible light, and could accelerate the application of photocatalytic membrane in practical circumstance. To the best of our knowledge, the present studies only concentrated on the photocatalysis of g-C_3N_4/Ag_3PO_4 nanocomposites; there is scant research on coupling membrane separation with g-C_3N_4/Ag_3PO_4 photocatalysis with visible light response for wastewater treatment in the literature.

In this work, novel g-C_3N_4/Ag_3PO_4-PVDF photocatalytic porous membranes were fabricated *via* phase inversion method with the utilization of visible-light-driven g-C_3N_4/Ag_3PO_4 nanocomposites as functional additives. The morphology, microstructure, chemical structure and hydrophilicity of the photocatalytic membranes were studied by relevant characterization by means of field-emission scanning electron microscopy (FESEM), atomic force microscopy (AFM), X-ray diffraction (XRD), Fourier transform infrared (FT-IR) spectrometry, electron spin resonance (ESR), contact angle analyses, and UV-vis absorption/diffuse spectra (DRS). The photocatalytic performance of the hybrid membranes was further investigated by using RhB as a model of pollutants under visible light conditions, and the results suggested that as-prepared nanocomposite membranes with low preparation cost, visible light response and satisfying photocatalytic activity may present an eco-friendly strategy that will be applied in environment wastewater treatment.

EXPERIMENTAL SECTION

1. Materials

Commercial polyvinylidene fluoride (PVDF Mn¼ 110,000 g·mol^{-1}, Solef 6010) power was purchased from Solvay Solexis (Changshu, China)). Arkema. Rhodamine B (AR, RhB) was purchased from Aladdin Reagent Ltd. Melamine, silver nitrate ($AgNO_3$), trisodium phosphate anhydrous (Na_3PO_4), melamine, dimethyl sulfoxide (DMSO) were purchased from Sinopharm Chemical Reagent Co., Ltd., China. Doubly distilled water was used in all cleaning processes and aqueous solutions in the experiments.

2. Preparation of g-C_3N_4 Sheets

Graphite-C_3N_4 sheets were prepared on the basis of a method reported previously [20]. In brief, 5.0 g of melamine was dried at 80 °C for 24 h in a crucible without a cover under ambient pressure in the air, then the precursor was calcined at 550 °C with a heating rate of 2.3 °C min^{-1} in a muffle furnace for 4 h in air. The obtained final yellow agglomerate was ground into powder.

3. Preparation of g-C_3N_4/Ag_3PO_4 Nanocomposites

g-C_3N_4/Ag_3PO_4 heterojunctions with different Ag_3PO_4 contents were synthesized according to the previously reported method [18]. In a typical procedure, 0.034 g of $AgNO_3$ was dispersed into 100 mL of pure water, and then 80 mg of g-C_3N_4 was added into the above solution by ultrasonication. The mixture was vigorously stirred for 1.0 h. Then 50 mL of 0.507 g L^{-1} prepared freshly Na_3PO_4 aqueous solution was put dropwise into the mixture; the reaction mixture was continually stirred for another 1.0 h. The mixture was then collected by centrifugation at 8,000 rpm, washed with pure water and dried by a vacuum drier at 45 °C. As a comparison, Ag_3PO_4 nanoparticles were also prepared in the absence of C_3N_4 nanosheets by the same method as with g-C_3N_4/Ag_3PO_4 heterojunction. In this manner, different mass ratios of the g-C_3N_4 to Ag_3PO_4 samples (abbreviated as g-C_3N_4/Ag_3PO_4 (17%), g-C_3N_4/Ag_3PO_4 (34%) and

Table 1. Membrane composition for all prepared PVDF blend membranes

Membrane	Polymer (wt%) (PVDF)	Additives		Solvent (wt%) DMSO
		Nanomaterials	Amounts (wt%)	
PVDF	10	-	-	90
g-C_3N_4-PVDF	10	g-C_3N_4	2	88
g-C_3N_4/Ag_3PO_4-PVDF	10	g-C_3N_4/Ag_3PO_4	2	88

g-C_3N_4/Ag_3PO_4 (68%)) were obtained. All the experiments were completed at room temperature.

4. Preparation of g-C_3N_4/Ag_3PO_4/PVDF Photocatalytic Membranes

The PVDF-based photocatalytic membranes were prepared by incorporating g-C_3N_4/Ag_3PO_4 heterojunction by phase inversion technique. In brief, an appropriate amount of g-C_3N_4/Ag_3PO_4 nanoparticles were dispersed into DMSO by ultrasonication for 30 min, then PVDF power was added into the above solution with a constant magnetic stirring for 12 h at 50 °C to form homogeneous casting solution, and then stored for another 12 h at 50 °C to remove the air bubbles. After that, the as-prepared solution was cast on an undefiled glass plate using a doctor knife, then was instantly immersed into a coagulant bath containing deionized water. Upon complete coagulation, the different membranes were put into deionized water for solvent-exchange process. The as-prepared photocatalytic membranes were stored in deionized water for further utilization. For comparison, the original PVDF membranes and g-C_3N_4-PVDF membranes were prepared by the same method. The PVDF blend membranes were prepared according to composition given in Table 1.

5. Characterization

The crystal structure and phase purity of the obtained samples were measured by X-ray diffraction (XRD, Rigaku, Smartlab, operated at 40 kV and 200 mA, Cu Kα source) at a scanning speed of 7.0° min^{-1} in the 2θ range from 10 to 80°. The morphology of different membranes was observed by field-emission scanning electron microscope (FE-SEM, JSM-6010PLUS/LA) and atomic force microscope (AFM, Agilent PicoPlus), respectively. UV-vis diffuse reflectance spectra were recorded on a Shimadzu UV-2450 spectrophotometer equipped with spherical diffuse reflectance accessory. Fourier transform spectrophotometer (FT-IR, Nexus 470, Thermo Electron Corporation) was used to characterize the functional groups of different membranes.

6. Photocatalytic Activity

The photocatalytic activity of the as-prepared samples was examined by the degradation of RhB in aqueous solution (10 mg/L) under visible light irradiation. And a 200 W Xenon lamp with a 420 nm cutoff filter was used as the light source of the photocatalytic reaction. Briefly, 50 mg of as-synthesized photocatalysts with recycling water (25 °C) to maintain a constant reactor temperature. Prior to irradiation, the suspension was magnetically stirred in 50 mL pollutant aqueous solution (10 mg/L) for 40 min in the dark to achieve absorption-desorption equilibrium on the photocatalyst powders. During photocatalytic reaction, a 5 mL solution was collected from photodegraded dye solution and centrifuged to separate the photocatalysts at 20 min intervals. The filtrates were monitored by UV-vis spectrophotometer, and the characteristic absorption peak of RhB at 554 nm was used to determine the extent of its degradation.

7. Membrane Performance Tests

7-1. Porosity Study of Membranes

The porosity of prepared membranes was evaluated by using gravimetric method as expressed in the following equation [36] (Eq. (1)):

$$\varepsilon(\%) = \frac{\dfrac{(W_w - W_d)}{\rho_H}}{\dfrac{(W_w - W_d)}{\rho_H} + \dfrac{W_d}{\rho_c}} \quad (1)$$

where W_w is the weight of wet membranes and W_d is the weight of the dry membranes (g). ρ_H and ρ_c are the density of water (0.998 g cm^{-3}) and PVDF (1.77 g cm^{-3}), respectively.

7-2. Permeation and Fouling Study of Membranes

The membrane permeation flux and antifouling properties were conducted with an effective area of 3.14 cm^2 using an ultrafiltration cell (UF-8010, Amicon) for 1.0 h [37]. The pure water permeated through various membranes and the membrane flux could be calculated by Eq. (2):

$$J = \frac{Q}{AT} \quad (2)$$

where J is the flux of the various membranes (L m^{-2} h^{-1}), Q is the volume of permeate pure water (mL), T and A are the operation time (min) and effective area of the membranes (cm^2), respectively.

The antifouling performance of the prepared membranes was evaluated through a static protein adsorption test (bovine serum albumin (BSA) solution was selected as a model protein) [38]. Typically, a 9 cm^2 piece of each membrane was put into 10 mL of BSA solution (1.0 g L^{-1}) for 24 h to reach adsorption-elution equilibrium at room temperature. The initial and the final concentrations of BSA in the solution were obtained by UV-vis spectrophotometry at a wavelength of 280 nm. The BSA adsorption capacity of the membrane was calculated by Eq. (3):

$$Q = \frac{(C_0 - C_t) \cdot V}{S} \quad (3)$$

where C_0 and C_t are the initial and equilibrium concentrations of BSA, V (mL) is the volume of BSA solution and S (cm^2) is the adsorption area of membranes. The average of at least three measurements was reported.

To further analyze the anti-fouling process, the flux recovery ratio (FRR) was also computed to describe the fouling resistance of the prepared membranes and expression using Eq. (4), respectively [39].

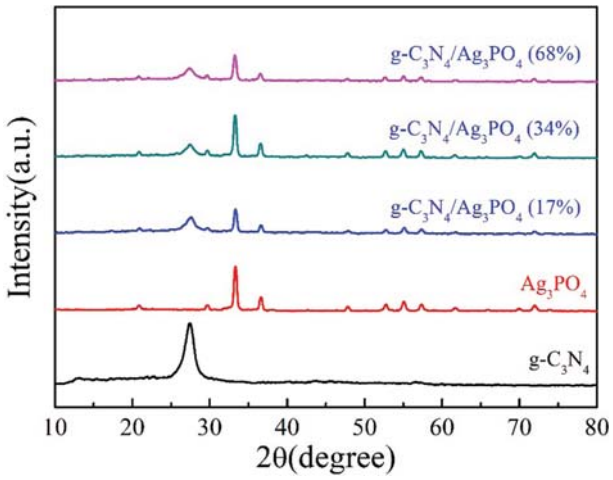

Fig. 1. XRD patterns. The line marks g-C_3N_4, Ag_3PO_4, g-C_3N_4/Ag_3PO_4 (17%), g-C_3N_4/Ag_3PO_4 (34%) andg-C_3N_4/Ag_3PO_4 (68%).

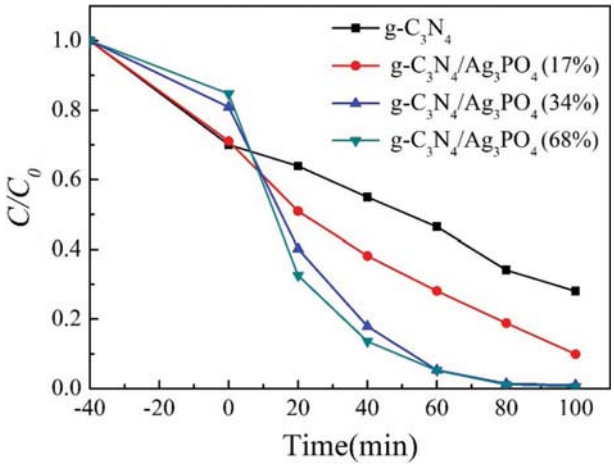

Fig. 3. Photodegradation of RhB under visible-light irradiation for g-C_3N_4, g-C_3N_4/Ag_3PO_4 (17%), g-C_3N_4/Ag_3PO_4 (34%) and g-C_3N_4/Ag_3PO_4 (68%) powder.

$$FRR = \left(\frac{J_2}{J_1}\right) \times 100 \quad (4)$$

where J_1 is the pure water flux before the BSA fouling test, J_2 is the pure water flux after fouling.

RESULTS AND DISCUSSION

1. Morphology and Structure of g-C_3N_4 and g-C_3N_4/Ag_3PO_4 Nanocomposites

Powder XRD patterns of pure-C_3N_4, pure Ag_3PO_4, g-C_3N_4/Ag_3PO_4 (17%), g-C_3N_4/Ag_3PO_4 (34%) and g-C_3N_4/Ag_3PO_4 (68%) are shown in Fig. 1. Clearly, the pure g-C_3N_4 exhibits a strong peak at 27.4°, corresponding to the characteristic interlayer stacking peak of aromatic systems, that could be indexed as (002) diffraction plane, which is well known for the melon networks. As for the pure Ag_3PO_4 sample, all the peaks could be well indexed to the cubic phase (JCPDS 65-0309). The samples exhibited obvious diffraction peaks at 2θ=20.8°, 29.7°, 33.3°, 36.6°, 47.8°, 52.7°, 55.1°, 57.3°, 61.7°, 69.9°, 71.9° and 73.6°, which could be indexed to the (110), (200), (210), (211), (310), (222), (320), (321), (400), (420), (421) and (332) crystal planes, respectively. The g-C_3N_4/Ag_3PO_4 composites with different compositions presented similar diffraction patterns, corresponding to g-C_3N_4 and Ag_3PO_4, indicating the formation of g-C_3N_4 and Ag_3PO_4 composite. The above results indicated that the g-C_3N_4/Ag_3PO_4 nanocomposites had been successfully prepared.

The TEM of g-C_3N_4 and g-C_3N_4/Ag_3PO_4 composite is shown in Fig. 2. The bare g-C_3N_4 consists of many sheets with lamellar morphology, and the Ag_3PO_4 in the g-C_3N_4/Ag_3PO_4 samples was anchored evenly over the g-C_3N_4 substrate. The above results showed that the g-C_3N_4/Ag_3PO_4 nanocomposites were successfully prepared.

2. Photocatalytic Activity of g-C_3N_4/Ag_3PO_4 Nanocomposites

The photocatalytic activity of as-prepared samples was examined by the degradation of RhB in aqueous solution (10 mg/L) under irradiation of a 200 W xenon light lamp ($\lambda \geq 420$ nm). Fig. 3 shows the variation in concentration of RhB (C/C_0) with irradiation time over different photocatalysts, where C_0 is the initial concentration of RhB and C is its concentration at time t. Prior to irradiation, the suspension was magnetically stirred for 40 min in the dark to reach the absorption-desorption equilibrium on the photocatalyst pow-

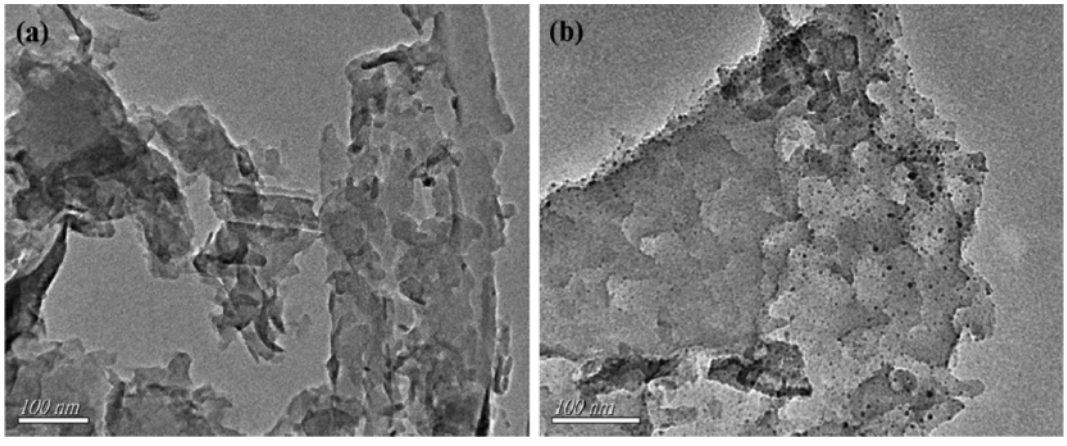

Fig. 2. TEM images of g-C_3N_4 (a) and g-C_3N_4/Ag_3PO_4 (b).

ders. Clearly, g-C_3N_4/Ag_3PO_4 (34%) and g-C_3N_4/Ag_3PO_4 (68%) had weaker adsorptive ability of RhB due to more Ag_3PO_4 loading counts on the g-C_3N_4 nanosheets, decreasing the specific surface area and adsorption capacity of the g-C_3N_4 sheets. Under visible light irradiation, the pure g-C_3N_4 exhibited a relatively weak photocatalytic activity that could degrade only 60% RhB. With the loading of different molar ratios of Ag_3PO_4 on the surface of g-C_3N_4, all the g-C_3N_4/Ag_3PO_4 nanocomposites showed higher photocatalytic ability for degrading RhB compared with the pure g-C_3N_4. t g-C_3N_4/Ag_3PO_4 (34%) and g-C_3N_4/Ag_3PO_4 (68%) clearly showed the optimal photocatalytic activity for the decolorization of RhB under visible-light irradiation (g-C_3N_4/Ag_3PO_4 (34%), about 98%, g-C_3N_4/Ag_3PO_4 (68%), about 99%). This could be because of interfacial charge transfer between g-C_3N_4 and isolated larger Ag_3PO_4 particles, which could reduce the probability of electron-hole recombination, improve the separation efficiency of the photoinduced electron hole pairs, and further enhance the photocatalytic activity. Furthermore, according to the results of photocatalytic activity of g-C_3N_4/Ag_3PO_4 nanocomposites, considering the cost of the experiment, in the following tests analysis we used g-C_3N_4/Ag_3PO_4 (34%) as optimal photocatalyst.

3. Morphology and Structure of Membranes

FT-IR was used to examine the changes of functional groups of the pristine PVDF, g-C_3N_4-PVDF and g-C_3N_4/Ag_3PO_4-PVDF membranes by using FT-IR spectra. As shown in Fig. 4, the pristine PVDF membranes exhibit a strong and sharp absorption peak at 1,404 cm^{-1}, which was attributed to the stretching vibrations of C-H. The peak located at 1,176 cm^{-1} belongs to the vibration of C-F. The emerging peaks at 1,637 cm^{-1} of g-C_3N_4-PVDF membranes are attributable to C=N stretching vibration modes of g-C_3N_4, The

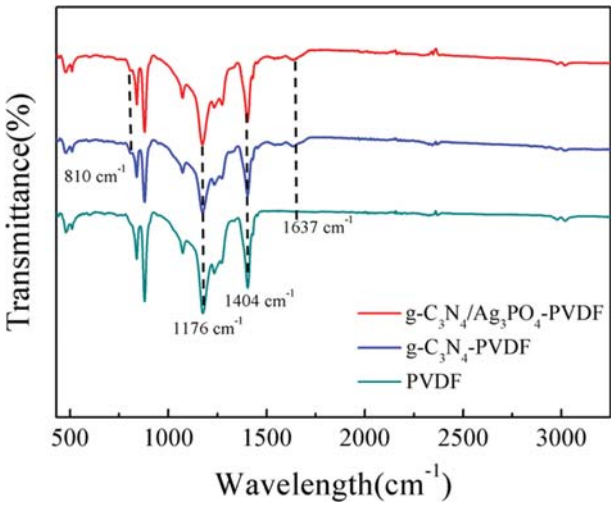

Fig. 4. FT-IR spectra of pristine PVDF, g-C_3N_4-PVDF and g-C_3N_4/Ag_3PO_4-PVDF membranes.

FT-IR spectra of samples show the typical stretching modes of g-C_3N_4 heterocycles in the 1,200-1,650 cm^{-1} range; the peaks at 1,234, 1,316, 1,454 and 1,542 cm^{-1} could be ascribed to aromatic C-N stretching vibration modes. The peak at 810 cm^{-1} is related to the characteristic breathing mode of s-triazine units. The FT-IR spectra of all the doped g-C_3N_4 samples, the characteristic peaks of g-C_3N_4 did not change after combination with Ag_3PO_4. However, the FT-IR spectra of g-C_3N_4/Ag_3PO_4-PVDF membranes show no obvious characteristic peaks of Ag_3PO_4, which was also attributed to the relatively low quantity of Ag_3PO_4 or overlap with other peaks.

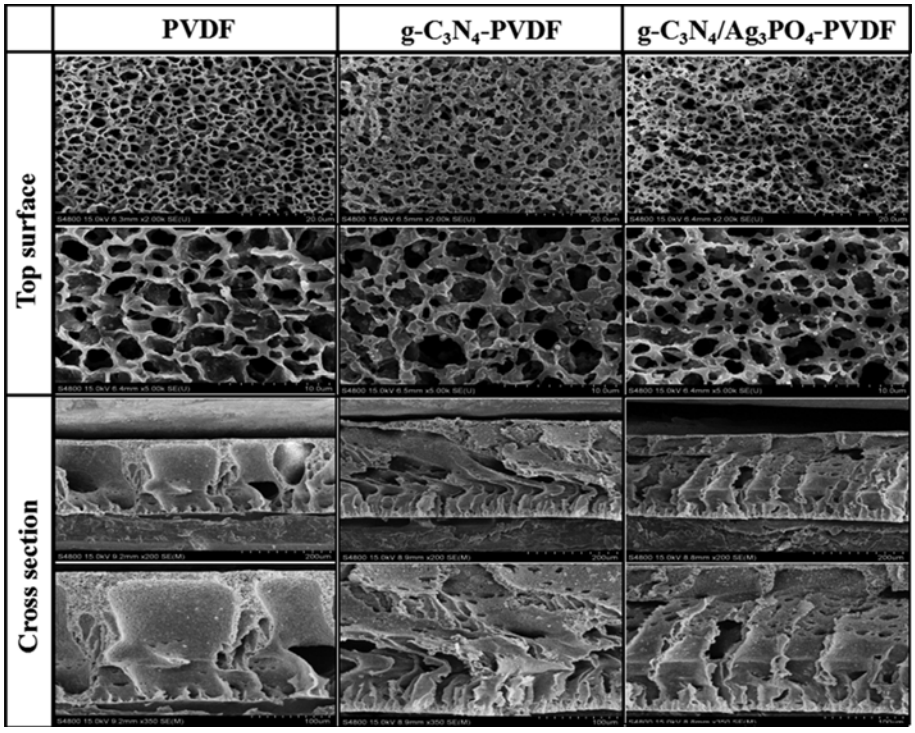

Fig. 5. SEM images of top surface and cross section morphologies of PVDF, g-C_3N_4-PVDF and g-C_3N_4/Ag_3PO_4-PVDF membranes.

The above results indicate that the g-C_3N_4/Ag_3PO_4-PVDF membranes were successfully prepared by the phase inversion technique developed here.

SEM images were taken to determine the influence of inorganic nanocomposites on the morphology of PVDF membrane. As observed in Fig. 5, all prepared PVDF nanocomposite membranes exhibited a typically porous structure; meanwhile, the nanocomposite membranes showed no obvious agglomerates of g-C_3N_4 and g-C_3N_4/Ag_3PO_4, which illustrated that they were well dispersed in the PVDF matrix before casting. The addition of inorganic nanomaterials also increased the binding affinity of the PVDF solution towards the water, further improved the rate of demixing, in turn; it was visually viewed that g-C_3N_4/Ag_3PO_4-PVDF membranes exhibited the more macroporous substructures and larger surface macrovoids from the SEM pictures. In addition, the cross sections of as-prepared hybrid membranes wider pore channels formers were also investigated, all the membranes displayed a typical asymmetric microstructure including a thin dense skin layer supported by numerous finger-like macrovoids. These are attributed to the prompt exchange between the solvent and non-solvent during the phase inversion process, which was ameliorated by presence of the hydrophilic nature of g-C_3N_4 and g-C_3N_4/Ag_3PO_4 inorganic nanocomposites. These results were also consistent with the porosity depicted in the Table 2; it was observed that the g-C_3N_4/Ag_3PO_4-PVDF mem-

Table 2. Porosity, water contact angle, pure water flux, FRR and roughness parameters of various membranes

Membrane	Porosity (%)	Water contact angle (°)	Pure water flux ($L \cdot m^{-2} \cdot h^{-1}$)	FRR	Roughness	
					Ra (nm)	Rq (nm)
PVDF	73	97	541	41	492	597
g-C_3N_4-PVDF	79	82	1025	62	392	505
g-C_3N_4/Ag_3PO_4-PVDF	85	79	1083	74	319	417

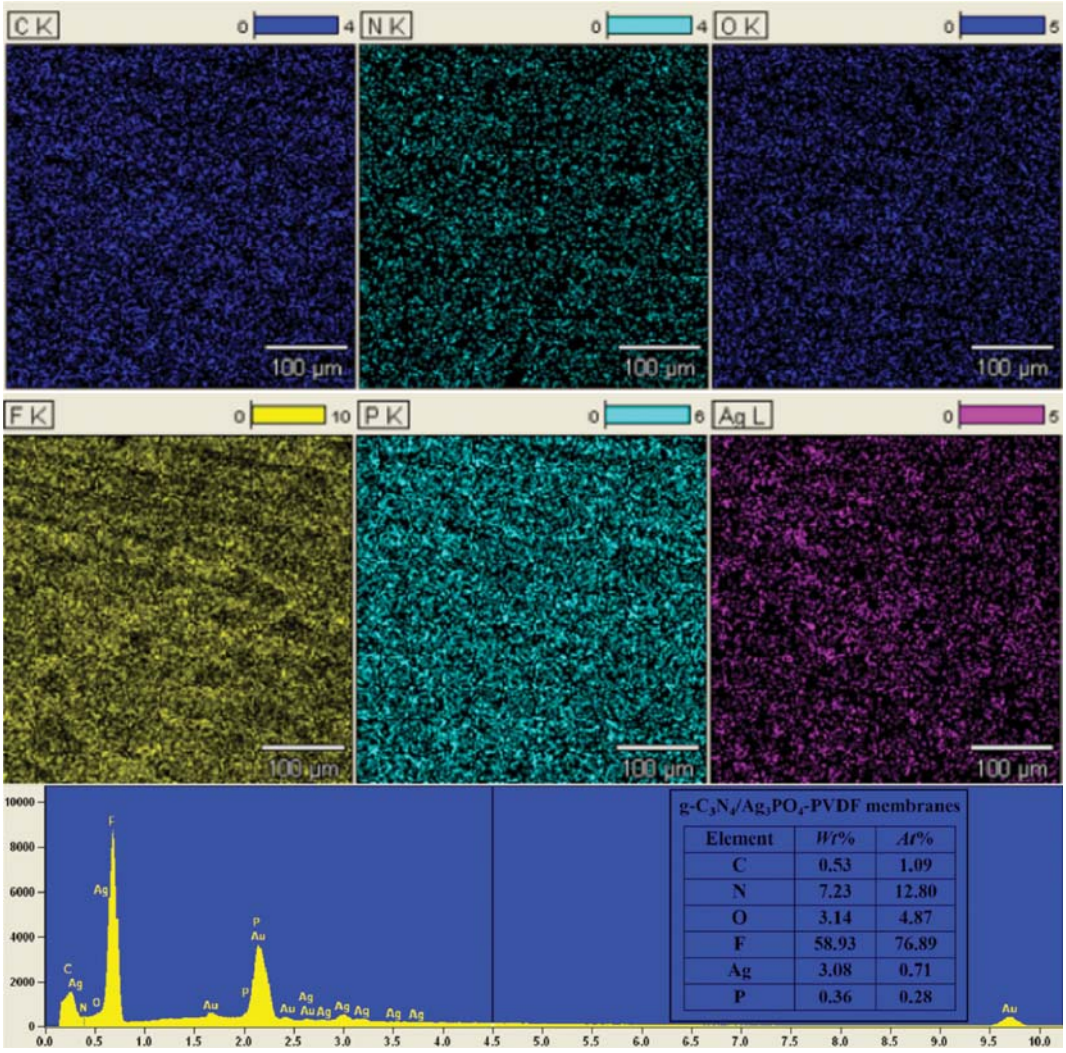

Fig. 6. EDX mapping scanning spectrum of g-C_3N_4/Ag_3PO_4-PVDF membranes.

branes expressed higher porosity than the other two control membranes, which could be attributed to the effect of supplementing with g-C_3N_4/Ag_3PO_4 nanocomposites into the membrane matrix and forming interfacial pores of the organic phase shrinkage.

Furthermore, to investigate the presence and dispersion uniformity of g-C_3N_4/Ag_3PO_4 nanocomposites in the PVDF membrane matrix, the SEM-EDX mapping scanning spectrum for g-C_3N_4/Ag_3PO_4-PVDF membranes surface of carbon (C), nitrogen (N), oxygen (O), fluorine (F), phosphorus (P) and silver (Ag) elements was carried out in Fig. 6. Note that the C, N, Ag, O and P elements are evenly distributed in the g-C_3N_4/Ag_3PO_4-PVDF membranes, indicating the homogeneous dispersion of g-C_3N_4/Ag_3PO_4 nanocomposites within the PVDF membrane matrix.

AFM optical photographs were used to detect the surface microstructure of various synthesized membranes, and the results are shown in Fig. 7. All the AFM two-dimensional and 3D images of PVDF, g-C_3N_4-PVDF and g-C_3N_4/Ag_3PO_4-PVDF membranes were porous surface, which is well consistent with the results of SEM analysis. The 3D images of different membranes are also shown in Fig. 7, while the corresponding roughness parameters are presented in Table 2. From these data, the surface roughness of the nanocomposite membranes displayed an apparent decreasing trend in contrast to that of original PVDF membranes. For instance, Ra value of PVDF membranes was 492 nm; after blending inorganic nanomaterials, Ra value of g-C_3N_4-PVDF and g-C_3N_4/Ag_3PO_4-PVDF membranes decreased to 392 nm and 319 nm, respectively. These observed decreases in surface roughness are probably attributed to the rapid exchange of solvent and non-solvent occurring during the phase inversion process due to the presence of hydrophilic inorganic nanomaterials. Xu et al. [40] also reported GO/TiO_2-PVDF hybrid membranes had the similar behavior.

The optical absorption properties of pure PVDF, g-C_3N_4-PVDF and g-C_3N_4/Ag_3PO_4-PVDF membranes were studied by the UV-vis absorption/diffusion spectra (DRS), and the results are displayed in Fig. 8. The basal absorption edge of the original PVDF membranes that occurred at about 274 nm did not absorb light between 275 and 800 nm. In comparison to the pure PVDF membranes, the band edge positions of g-C_3N_4-PVDF membranes showed a large red shift, and the results indicated that g-C_3N_4-PVDF membranes could absorb UV-vis light. Compared with g-C_3N_4-PVDF membranes, the absorption intensity of g-C_3N_4/Ag_3PO_4-PVDF membranes had obvious enhancement in the whole visible region, which indicates that it could absorb the whole range of light. This phenomenon is attributed to the presence of Ag_3PO_4 nanocomposites with a deep color characteristic. Therefore, the results of DRS demonstrate that g-C_3N_4/Ag_3PO_4-PVDF membranes could

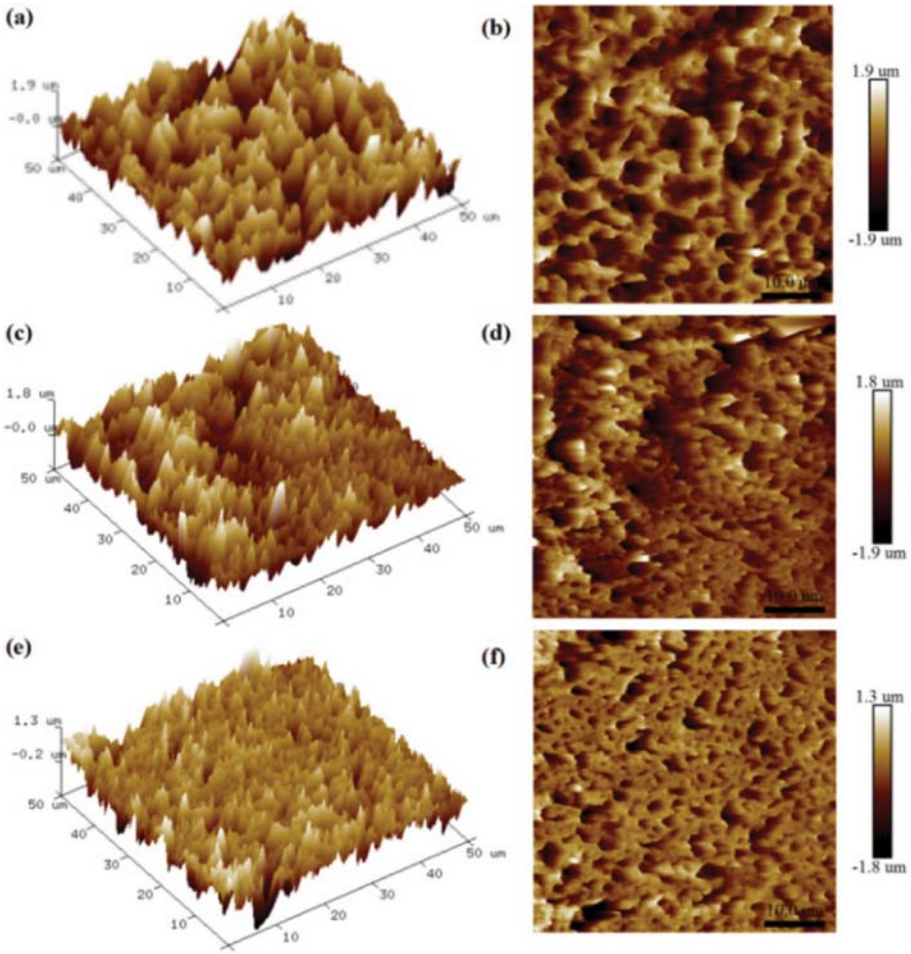

Fig. 7. AFM images of (a), (b) the original PVDF and (c), (d) g-C_3N_4-PVDF (e), (f) g-C_3N_4/Ag_3PO_4-PVDF membranes.

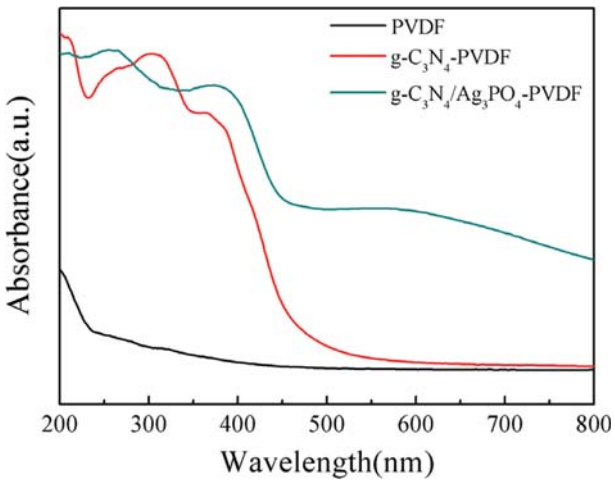

Fig. 8. UV-vis absorption spectra of the as-prepared various membrane.

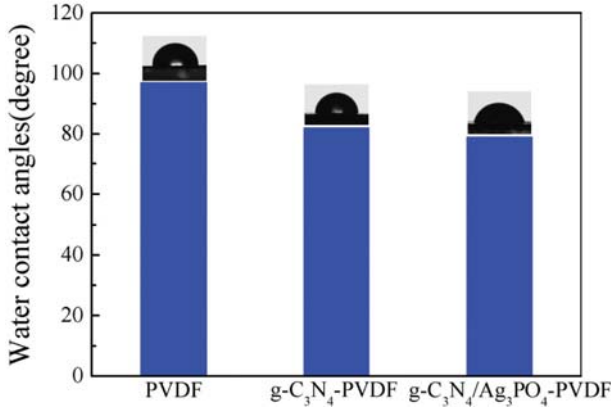

Fig. 9. Water contact angle of various membranes.

improve the absorption of visible light and offer proper reaction conditions for photocatalytic degradation.

4. Hydrophilicity of Membranes

Surface hydrophilicity is an important factor in determining the permeability and antifouling performance of photocatalytic membranes, which was analyzed with water contact angle measurement by the sessile drop technique. It is indeed noticeable that a smaller contact angle value shows greater hydrophilicity [41]. As shown in Fig. 9, the contact angle of pure PVDF membranes clearly has the highest value than the other two control membranes; from Table 2, the values of g-C_3N_4-PVDF and g-C_3N_4/Ag_3PO_4-PVDF membranes are decreased to 82° and 79°, respectively. This is mainly attributed to the supplementation of hydrophilic nanomaterials blending into the pure PVDF membranes, which future facilitates the water molecules to pass through the membranes and makes the hybrid membranes more hydrophilic.

5. Permeation and Antifouling Properties of Membranes

The membrane permeation performance was determined through testing pure water flux, and the results are shown in Fig. 10, which suggests that all the composite membranes supplemented with inorganic nanomaterials presented higher water permeation flux

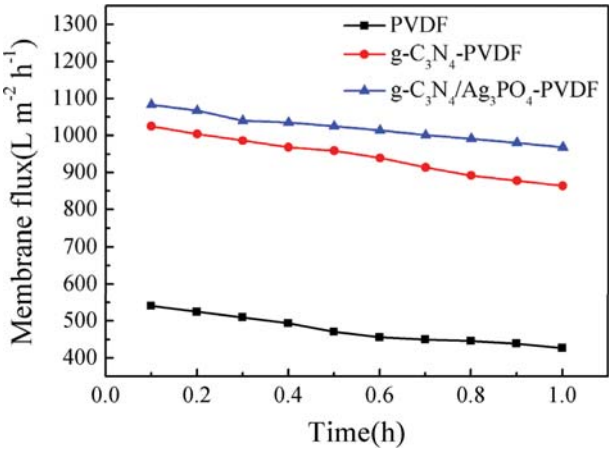

Fig. 10. Pure water flux of various membranes.

compared with pure PVDF membranes, future indicating that the nanocomposite membranes had high hydrophilicity and anti-fouling property. As illustrated in Table 2, the pure PVDF membranes had the lowest pure water flux value of 541 $L \cdot m^{-2} \cdot h^{-1}$, with the inorganic nanomaterials blending into the original PVDF membranes; the pure water flux of g-C_3N_4/Ag_3PO_4-PVDF membranes was 1,083 $L \cdot m^{-2} \cdot h^{-1}$, of g-$C_3N_4$-PVDF membranes was 1,025 $L \cdot m^{-2} \cdot h^{-1}$. This improvement in water flux may be attributed to the coupling effects of supplementation of the membrane matrix with g-C_3N_4 and g-C_3N_4/Ag_3PO_4 nanomaterials, which demonstrated that g-C_3N_4 and g-C_3N_4/Ag_3PO_4 nanoparticles on the membrane surface decreased the interaction between the contaminants and the membrane surface and made the membrane more hydrophilic, then facilitated the water molecules to pass through the membrane. In addition, all the water flux values decreased attributed to jammed inner pores, It also can be seen that the pure PVDF, g-C_3N_4-PVDF and g-C_3N_4/Ag_3PO_4-PVDF membranes decreased nearly 20%, 15%, 10% of the membrane flux of the study within 1.0 h from Fig. 10, respectively. It is believed that all the composite membranes supplemented with inorganic nanomaterials led to lower flux decline and higher antifouling performance. In this study, g-C_3N_4/Ag_3PO_4-PVDF membranes showed high permeation and good antifouling performance.

A static BSA adsorption test was one of the dominant factors to determine the fouling properties of as-prepared membranes [42]. As shown in Fig. 11(a), it suggested that a clear trend that the polymer membranes blended with inorganic materials caused the decrease of BSA adsorption, and g-C_3N_4/Ag_3PO_4-PVDF membranes revealed the lowest BSA adsorption capacity of 0.06 mg/cm^2, lower than g-C_3N_4-PVDF of 0.11 mg/cm^2, PVDF of 0.24 mg/cm^2, respectively. These results could be due to the presence of hydrophilic particles into membrane matrix, enhancing the polar surface of the membranes, further improving electrostatic repulsion to BSA and lessening membrane fouling. In addition, FRR was measured to comprehensively monitor various membranes fouling. As can be obviously seen from Fig. 11(b), FRR of nanocomposites membranes was clearly higher than that of pure PVDF membranes. The pristine PVDF membranes displayed the lowest FRR of 41%, implying a poor antifouling property. The addition of g-C_3N_4 and

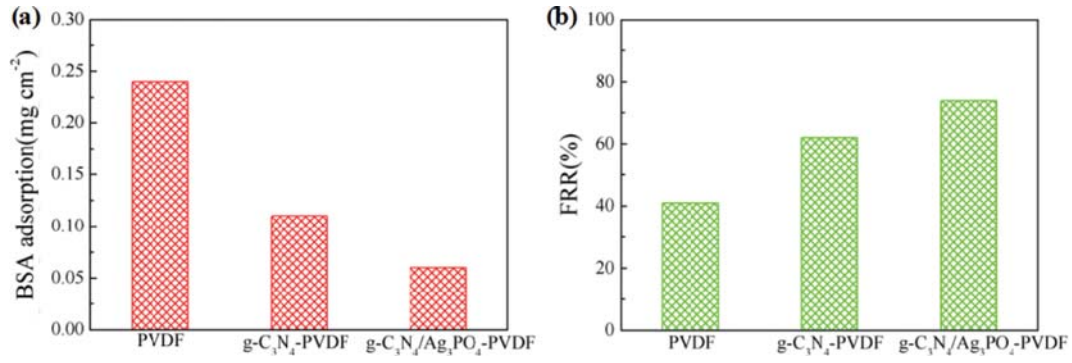

Fig. 11. Static BSA adsorption (a) and FRR of various membranes.

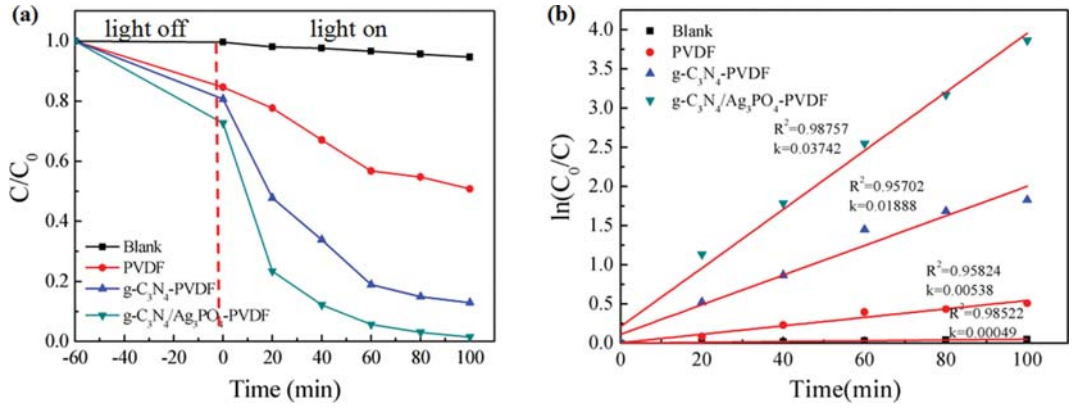

Fig. 12. Photodegradation of RhB under visible-light irradiation (a) and the corresponding kinetic linear simulation curves (b) over the synthesized membranes.

g-C_3N_4/Ag_3PO_4 enhanced the FRR to 62% and 74%, respectively, suggesting improved antifouling properties due to better hydrophilicity. Therefore, the g-C_3N_4/Ag_3PO_4-PVDF membranes had excellent fouling resistance.

6. Photocatalytic Properties of Membranes

The photocatalytic performance of g-C_3N_4/Ag_3PO_4-PVDF membranes was tested by removing RhB aqueous solution (10 mg/L) under irradiation of a 200 W xenon light lamp. Fig. 12(a) shows the variation in concentration of RhB (C/C_0) with irradiation time over different membranes, where C_0 is the initial concentration of RhB and C is its concentration at time t. As described in Fig. 12(a), the blank test showed that RhB was only slightly removed in the absence of catalysts, indicating that the photolysis of RhB could be negligible. And for the pure PVDF membranes, RhB was decreased to 59% in 100 min, but the optical absorption properties of pure PVDF membranes did not absorb light between 275 and 800 nm. It could be considered that the pristine PVDF membranes only absorb RhB; the removal ratio of RhB was 41% under visible-light irradiation. In comparison, photocatalytic activity of g-C_3N_4-PVDF and g-C_3N_4/Ag_3PO_4-PVDF membranes for RhB was significantly improved under the visible-light irradiation; the removal rates for g-C_3N_4-PVDF and g-C_3N_4/Ag_3PO_4-PVDF membranes were 85%, 98%, respectively. In addition, as shown in Fig. 12, almost 27% of RhB was removed using membrane separation alone without light irradiation, while more than 92% of RhB removal was obtained by the photo-assisted g-C_3N_4/Ag_3PO_4-PVDF membranes, which was about three-times than that of permeation alone under the same time of 60 min. For comparison, the use of g-C_3N_4-PVDF membranes without Ag_3PO_4 layer under light irradiation only removed 76% of RhB. These results evidenced that the g-C_3N_4/Ag_3PO_4-PVDF membranes had a good removal capability with the synergistic effect of membrane separation and photocatalysis.

To further understand the reaction kinetics of RhB removal under photo-assistance, the apparent pseudo-first-order model was fitted according to the equation $\ln(C_0/C)=kt$ (Fig. 12(b)), where k is the apparent first-order rate constant (min^{-1}), C_0 is the initial RhB concentration in aqueous solution (mg/L), C is the RhB concentration at time (mg/L). The high coefficient of measurement ($R^2>0.9$) showed that the catalytic reaction was well fitted to the pseudo-first-order reaction kinetics. The k of g-C_3N_4/Ag_3PO_4-PVDF membranes could reach 0.03742 min^{-1}, which was larger than blank (0.00049 min^{-1}), PVDF membranes (0.00538 min^{-1}), g-C_3N_4-PVDF membranes (0.01888 min^{-1}), respectively.

Photoluminescence (PL) spectroscopy was implemented to analyze photoinduced interfacial charge transfer processes in g-C_3N_4-PVDF and g-C_3N_4/Ag_3PO_4-PVDF membranes. As shown in Fig. 13(a), the emission peak intensity of g-C_3N_4/Ag_3PO_4-PVDF membranes was lower than that of g-C_3N_4-PVDF membranes, which further indicates that the recombination of photoinduced electron-

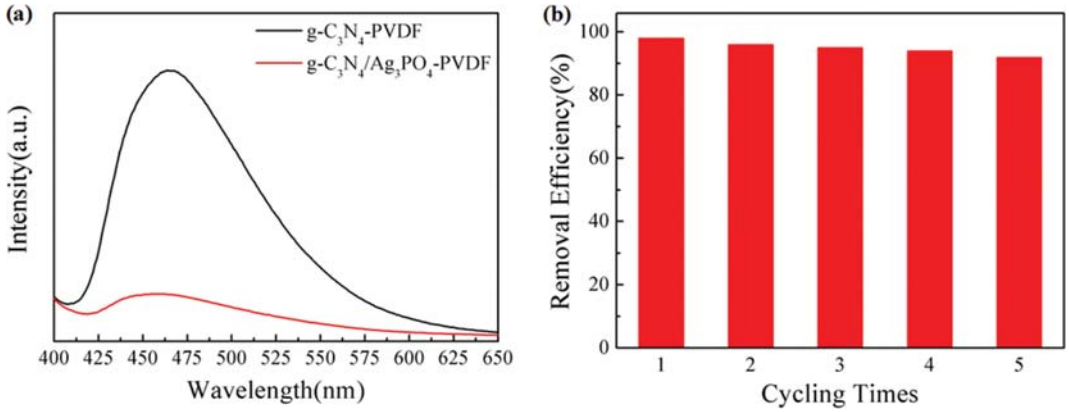

Fig. 13. PL spectra of the g-C_3N_4-PVDF and g-C_3N_4/Ag_3PO_4-PVDF membranes (a); Cycling test and reusability of g-C_3N_4/Ag_3PO_4-PVDF membranes under visible-light irradiation (b).

hole pairs of g-C_3N_4/Ag_3PO_4-PVDF membranes were greatly restrained. Therefore, the effective charge separation at the heterojunction interface on g-C_3N_4/Ag_3PO_4-PVDF membranes showed higher photocatalytic activity than g-C_3N_4-PVDF membranes.

We also studied g-C_3N_4/Ag_3PO_4-PVDF membrane renewability over repeating photocatalytic degradation of RhB. After each experiment, the membranes were washed for 30 min in water for the next catalytic experiment. As shown in Fig. 13, the removal efficiency of g-C_3N_4/Ag_3PO_4-PVDF membranes was almost unchanged after fifth cycle experiments, which indicates that the g-C_3N_4/Ag_3PO_4-PVDF membranes exhibited good stability and regeneration capacity ascribed to their high photocatalytic activity.

7. Research on Photocatalytic Mechanism

To further detect the species of active radicals over g-C_3N_4/Ag_3PO_4-PVDF membranes during the degradation process, the electron spin resonance (ESR) spin-trap technique was applied. It is observed from Fig. 14 that there was no ESR signal in the dark. And the characteristic quadruple peaks of the DMPO-•OH adducts were extremely strong in water when the light was on (Fig. 14(a)). Meanwhile, the characteristic peaks of DMPO-•O^{2-} could be clearly detected in methanol, and the signal strength was also strong (Fig. 14(b)). These further confirmed the formation of •O^{2-} and •OH during the photocatalytic degradation of RhB process, which suggests that the •O^{2-} and •OH radicals simultaneously played important roles and were the main active species in the process of g-C_3N_4/Ag_3PO_4-PVDF membranes photocatalytic degradation of RhB.

On the basis of the above results, a possible photocatalytic mechanism for RhB photodegradation of g-C_3N_4/Ag_3PO_4-PVDF membranes is illustrated in detail in Fig. 15. Under the visible light illumination, due to band alignment and the potential difference, the reactions might be as follows. The original PVDF membranes only played a substrate support role in catalyst recovery and reuse. Catalyst layer of g-C_3N_4/Ag_3PO_4-PVDF membranes absorbed the visible light to produce photo-generated electrons (e^-) and photo-induced holes (h^+). The photo-generated electrons in the g-C_3N_4 conduction band (CB) quickly transferred towards the CB of Ag_3PO_4 due to the difference of CB edge potentials, while the holes on the valance band (VB) of Ag_3PO_4 could rapidly transfer towards the VB of g-C_3N_4, which conveniently made for an efficient separation of the photo-induced hole pairs. As a consequence, the efficient electron migration from Ag_3PO_4 to g-C_3N_4 could reduce the decomposition rates of Ag^+ to metallic Ag in the photocatalytic process so that the photolysis of Ag_3PO_4 could be alleviated. Subsequently, the photoelectrons could diffuse to the surface of Ag_3-

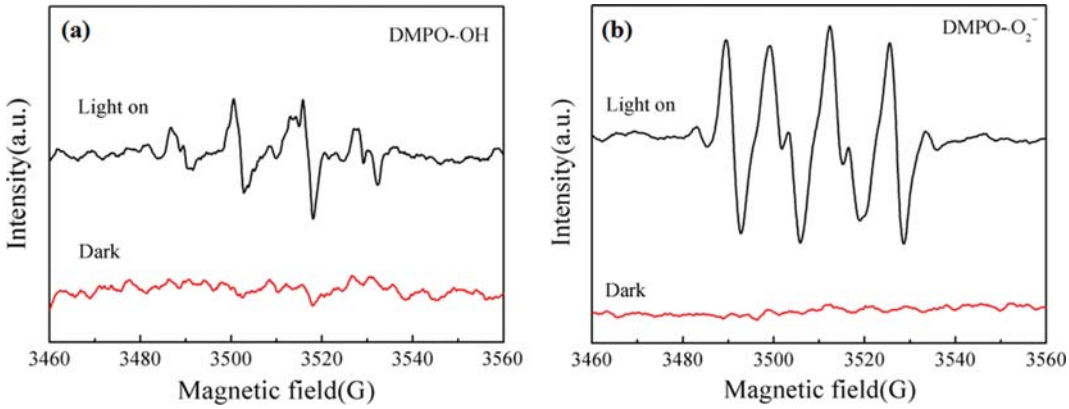

Fig. 14. ESR spectra of g-C_3N_4/Ag_3PO_4-PVDF membranes. (a) DMPO-•O^{2-} radical species was detected in methanol, (b) DMPO-•OH was detected in deionized water.

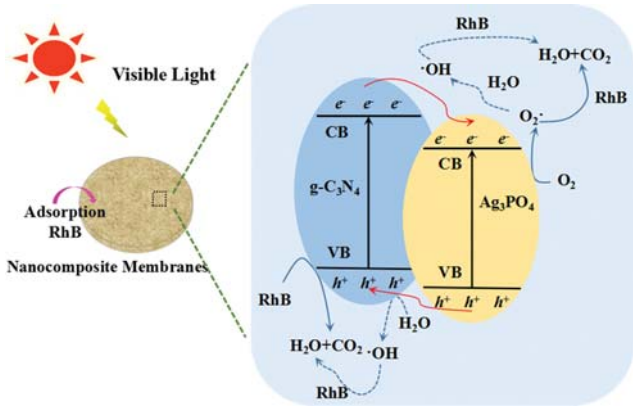

Fig. 15. Photocatalytic mechanism of degradation of RhB for g-C_3N_4/Ag_3PO_4-PVDF membranes.

PO_4 and reacted with the oxygen molecule to generate O^{2-}. And O^{2-} may transform H_2O to •OH. The •OH and O^{2-} are of high oxidation activity, which can oxidize RhB. In addition, the photo-generated holes on g-C_3N_4 could directly oxidize RhB. Moreover, holes could convert H_2O to •OH for degrading RhB. Thus, the photocatalytic activity of the g-C_3N_4/Ag_3PO_4-PVDF membranes could be improved due to the higher separation efficiency of photogenerated carriers.

CONCLUSIONS

Visible-light-driven g-C_3N_4/Ag_3PO_4-PVDF porous membranes were successfully developed by the phase inversion technique. Owing to the attractive photo-generated charge carrier separation efficiency of g-C_3N_4/Ag_3PO_4 heterojunction under visible light irradiation, the g-C_3N_4/Ag_3PO_4-PVDF photocatalytic membranes exhibited high performance for the removal of RhB in the coupling process of membrane separation with photocatalysis. The obtained g-C_3N_4/Ag_3PO_4-PVDF membranes exhibited higher porosity and lower surface roughness compared with pristine PVDF and g-C_3N_4-PVDF membranes. Moreover, the g-C_3N_4/Ag_3PO_4-PVDF membranes showed dramatic improvement in hydrophilicity and pure water permeability, resulting in increasing antifouling properties and separation performance, which is attributed to the implantation of g-C_3N_4/Ag_3PO_4 heterojunction in PVDF membrane matrix. Therefore, this study demonstrated that g-C_3N_4/Ag_3PO_4 was an efficient heterojunction structure for developing visible-light-responsive materials to improve wastewater treatment efficiency. In addition, the integration of photocatalysis with membrane separation technology is an ideal and efficient approach for future controlling the discharge of the organic contaminants into natural water bodies.

ACKNOWLEDGEMENTS

This work was financially supported by the National Natural Science Foundation of China (No. 21676127, 21808089, 21806060, 21776110, U1507118), the Natural Science Foundation of Jiangsu Province (No. BK20161367, BK20171315), the China Postdoctoral Science Foundation (Project No. 2014M561588, 1501067C, 170103B).

NOMENCLATURE

Symbols

T : time
A : area
C : concentration
R^2 : correlation coefficient
°C : degree centigrade
g : gram
h : hour
mg : milligram
mL : milliliter
mmol: millimole
moL : moore
FRR : flux recovery ratio
Q : volume
J : flux

Abbreviations

g-C_3N_4 : graphitic carbon nitride
DMSO : Dimethyl sulfoxide
Ag_3PO_4 : silver phosphate
RhB : rhodamine B
$AgNO_3$: silver nitrate
Na_3PO_4 : trisodium phosphate anhydrous
PVDF : polyvinylidene fluoride
SEM : scanning electron microscopy
AFM : atomic force microscope
DRS : UV-vis absorption/diffuse spectra
FT-IR : fourier infrared spectrum
XRD : X-ray diffraction
ESR : electron spin resonance

REFERENCES

1. G. L. Wang, S. Chen, H. T. Yu and X. Quan, *J. Hazard. Mater.*, **299**, 27 (2015).
2. H. Q. Wu, Y. J. Liu, L. Mao, C. H. Jiang, J. M. Ang and X. H. Lu, *J. Memb. Sci.*, **532**, 20 (2017).
3. K. G. Zhou, D. McManus, E. Prestat, X. Zhong, Y. Y. Shin, H. L. Zhang, S. J. Haigh and C. Casiraghi, *J. Mater. Chem. A*, **4**, 11666 (2016).
4. Z. W. Xu, T. F. Wu, J. Shi, K. Y. Teng, W. Wang, M. J. Ma, J. Li, X. M. Qian, C. Y. Cui and J. T. Fan, *J. Membr. Sci.*, **520**, 281 (2016).
5. Y. L. Wu, M. Yan, J. Y. Cui, Y. S. Yan and C. X. Li, *Adv. Funct. Mater.*, **25**, 5823 (2015).
6. N. Hamzah and C. P. Leo, *Desalination*, **418**, 79 (2017).
7. R. X. Zhang, L. Braeken, P. Luis, X. L. Wang and B. Van der Bruggen, *J. Membr. Sci.*, **437**, 179 (2013).
8. X. T. Wang, G. L. Wang, S. Chen, X. F. Fan, X. Quan and H. T. Yu, *J. Membr. Sci.*, **541**, 153 (2017).
9. Q. Zhang, X. Quan, H. Wang, S. Chen, Y. Su and Z. L. Li, *Sci. Rep.*, **7** (2017).
10. H. X. Zhao, S. Chen, X. Quan, H. T. Yu and H. M. Zhao, *Appl. Catal. B Environ.*, **194**, 134 (2016).
11. M. Kumar, Z. Gholamvand, A. Morrissey, K. Nolan, M. Ulbricht

and J. Lawler, *J. Membr. Sci.*, **506**, 38 (2016).
12. C. Wang, Y. L. Wu, J. Lu, J. Zhao, J. Y. Cui, X. L.Wu, Y. S. Yan and P. W. Huo, *ACS Appl. Mater. Interfaces*, **9**, 23687 (2017).
13. K. Fischer, M. Grimm, J. Meyers, C. Dietrich, R. Glaeser and A. Schulze, *J. Membr. Sci.*, **478**, 49 (2015).
14. H. Xu, M. M. Ding, W. Chen, Y. Li and K. Wang, *Sep. Purif. Technol.*, **195**, 70 (2018).
15. I. Horovitz, D. Avisar, M. A. Baker, R. Grilli, L. Lozzi, D. Di Camillo and H. Mamane, *J. Hazard. Mater.*, **310**, 98 (2016).
16. L. D. Li, J. Q. Yan, T. Wang, Z. J. Zhao, J. Zhang, J. L. Gong and N. J. Guan, *Nat. Commun.*, **6** (2015).
17. L. L. Qu, N. Wang, H. Xu, W. P. Wang, Y. Liu, L. D. Kuo, T. P. Yadav, J. J. Wu, J. Joyner, Y. H. Song, H. T. Li, J. Lou, R. Vajtai and P. M. Ajayan, *Adv. Funct. Mater.*, **27**, 31 (2017).
18. X. X. Li, T. Wan, J. Y. Qiu, H. Wei, F. H. Qin, Y. H. Wang, Y. J. Liao, Z. Y. Huang and X. C. Tan, *Appl. Catal. B Environ.*, **217**, 591 (2017).
19. Y. H. Feng, L. Liu, J. Zhang, H. Aslanb and M. D. Dong, *J. Mater. Chem. B*, **5**, 8631 (2017).
20. Y. Z. Hong, C. S. Li, D. Li, Z. Y. Fang, B. F. Luo, X. Yan, H. Q. Shen, B. D. Mao and W. D. Shi, *Nanoscale*, **9**, 14103 (2017).
21. Y. Z. Hong, C. S. Li, Z. Y. Fang, B. F. Luo and W. D. Shi, *Carbon*, **121**, 463 (2017).
22. F. He, G. Chen, Y. S. Zhou, Y. G. Yu, Y. Zheng and S. Hao, *Chem. Commun.*, **51**, 16244 (2015).
23. F. He, G. Chen, Y. G. Yu, Y. S. Zhou, Y. Zheng and S. Hao, *Chem. Commun.*, **51**, 6824 (2015).
24. J. J. Xue, S. S. Ma, Y. M. Zhou, Z. W. Zhang and M. He, *ACS Appl. Mater. Interfaces*, **7**, 9630 (2015).
25. Y. Z. Hong, Y. H. Jiang, C. S. Li, W. Q. Fan, X. Yan, M. Yan and W. D. Shi, *Appl. Catal. B Environ.*, **180**, 663 (2016).
26. Y. Z. Hong, C. S. Li, G. Y. Zhang, Y. D. Meng, B. X. Yin, Y. Zhao and W. D. Shi, *Chem. Eng. J.*, **299**, 74 (2016).
27. W. Wang, J. J. Fang, S. F. Shao, M. Lai and C. H. Lu, *Appl. Catal. B Environ.*, **217**, 57 (2017).
28. N. Zhang, J. Gao, C. H. Huang, W. Liu, P. Tong and L. Zhang, *Anal. Chim. Acta*, **934**, 122 (2016).
29. Y. Xu, Z. C. Fu, S. Cao, Y. Chen and W. F. Fu, *Catal. Sci. Technol.*, **7**, 587 (2017).
30. J. F. Ma, D. Q. Huang, W. Y. Zhang, J. Zou, Y. Kong, J. X. Zhu and K. Sridhar, *Chemosphere*, **162**, 269 (2016).
31. X. L. Miao, X. P. Shen, J. J. Wu, Z. Y. Ji, J. H. Wang, L. R. Kong, M. M. Liu and C. S. Song, *Appl. Catal. A Gen.*, **539**, 104 (2017).
32. L. Liu, Y. H. Qi, J. R. Lu, S. L. Lin, W. J. An, Y. H. Liang and W. Q. Cui, *Appl. Catal. B Environ.*, **183**, 133 (2016).
33. L. Zhou, W. Zhang, L. Chen, H. P. Deng and J. L. Wan, *Catal. Commun.*, **100**, 191 (2017).
34. J. F. Ma, D. Q. Huang, W. Y. Zhang, J. Zou, Y. Kong, J. X. Zhu and K. Sridhar, *Chemosphere*, **162**, 269 (2016).
35. M. Sun, Q. Zeng, X. Zhao, Y. Shao, P. G. Ji, C. Q. Wang, T. Yan and B. Du, *J. Hazard. Mater.*, **339**, 9 (2017).
36. M. Safarpour, A. Khataee and V. Vatanpour, *Sep. Purif. Technol.*, **140**, 32 (2015).
37. Z. H. He, M. J. Meng, L. Yan, W. H. Zhu, F. Q. Sun, Y. S. Yan, Y. Liu and S. J. Liu, *Sep. Purif. Technol.*, **145**, 63 (2015).
38. A. K. Ahmed, S. Leaper, M. Alberto, A. Vijayaraghavan, X. L. Fan, S. M. Holmes, E. R. Souaya, M. I. Badawy and P. Gorgojo, *Chem. Eng. J.*, **334**, 789 (2018).
39. Y. H. Xiang, F. Liu and L. X. Xue, *J. Membr. Sci.*, **476**, 321 (2015).
40. S. J. Xia and M. Z. Ni, *J. Membr. Sci.*, **473**, 54 (2015).
41. F. Li, Z. X. Yu, H. Shi, Q. B. Yang, Q. Chen, Y. Pan, G. Y. Zeng and L. Yan, *Chem. Eng. J.*, **322**, 33 (2017).